Growth and characterization of epitaxial ferroelectric lanthanum-substituted bismuth titanate nanostructures with three different orientations

Sung Kyun Lee,[a] Dietrich Hesse, Marin Alexe, Woo Lee, Kornelius Nielsch, and Ulrich Gösele
Max Planck Institute of Microstructure Physics, Weinberg 2, D-06120 Halle/Saale, Germany

(Received 9 August 2005; accepted 27 October 2005; published online 16 December 2005)

Well-ordered large-area arrays of ferroelectric La-substituted $Bi_4Ti_3O_{12}$ (BLT) nanostructures were prepared by pulsed laser deposition using gold nanotube membranes as shadow masks. By x-ray diffraction and transmission electron microscopy, it was found that well-defined (001)-, (118)/(100)-, and (104)-oriented BLT nanostructures were obtained on (001)-, (011)-, and (111)-oriented $SrTiO_3$ single crystal substrates covered with epitaxial $SrRuO_3$ electrode layers, respectively, through *ex situ* crystallization at 700 °C. Atomic force microscopy analyses revealed that the epitaxial BLT nanostructures maintain a height of about 100 nm and a lateral size of about 150 nm in spite of the postannealing process. The anisotropic ferroelectric properties of the BLT nanostructures of three different orientations were investigated by scanning force microscopy in piezoresponse mode. The highest effective remanent piezoresponse coefficient ($2d_{zz}$) of about 38.0 pm/V was observed in (118)/(100)-oriented BLT nanostructures, whereas (001)- and (104)-oriented nanostructures showed smaller $2d_{zz}$ values of 5.0 pm/V and 1.4 pm/V, respectively. © *2005 American Institute of Physics*. [DOI: 10.1063/1.2140870]

I. INTRODUCTION

Bismuth-layered perovskite oxides, such as $SrBi_2Ta_2O_9$ (SBT) (Ref. 1) and La-substituted $Bi_4Ti_3O_{12}$ (BLT) (Ref. 2) have been extensively studied both in view of their fundamental properties and for their possible application to nonvolatile ferroelectric random access memory (NV-FRAM) systems. In particular, BLT is a promising material for use in NV-FRAM devices since it has remarkable advantages in terms of low processing temperatures, high remanent polarization, and high fatigue endurance.[2,3] For high density NV-FRAMs in the gigabit range, individual ferroelectric capacitors should have both thickness and lateral dimensions below 100 nm. Moreover, in spite of the very small size these ferroelectric capacitors should retain their ferroelectric properties, or piezoelectric properties for microelectromechanical systems (MEMS). However, degradation of ferroelectric properties, such as reduction of switching polarization and asymmetry of ferroelectric hysteresis loop, was observed in small ferroelectric structures.[4–7] Ferroelectricity vanishes below a critical size due to a weakening of the cooperative driving force which depends on the interaction of neighboring permanent electric dipoles in a crystal lattice, and an increasing depolarizing electrostatic field caused by dipoles at the ferroelectric-metal interfaces.[8] It is therefore important to understand the ferroelectric properties of nanostructured bismuth-layered perovskite materials concerning both three-dimensional size effects and memory device applications.

Bismuth-layered perovskite materials have a highly anisotropic structure [SBT (orthorhombic): $a=0.5531$ nm, $b=0.5534$ nm, and $c=2.4984$ nm,[9] $Bi_4Ti_3O_{12}$ (pseudo-orthorhombic): $a=0.545$ nm, $b=0.541$ nm, and $c=3.283$ nm,[10] and $Bi_{3.25}La_{0.75}Ti_3O_{12}$ (pseudo-orthorhombic): $a=0.542$ nm, $b=0.541$ nm, and $c=3.271$ nm,[3] at room temperature] and hence their ferroelectric properties are also anisotropic, which makes them useful for use in, e.g., MEMS applications. Ferroelectric anisotropic properties of bismuth-layered perovskites have been demonstrated in epitaxial thin films having different crystallographic orientations with respect to the substrate surface normal.[3,11–15] However, there are only a few reports on anisotropic properties in epitaxial nanostructures of these materials.[16]

For studies on the scaling behavior of nanostructured ferroelectrics as well as for real applications requiring large-area fabrication of ferroelectric capacitor arrays, several methods have been employed to produce nanostructured ferroelectric arrays, including electron beam (EB) direct writing, focused ion beam milling, self-patterning methods, and nanosphere lithography.[17–20] EB lithography is the most common technique to fabricate regular nanodot arrays but it has some drawbacks such as a low throughput due to its exposure time, restriction of resist materials, as well as the high cost of equipment. Recently, highly ordered nanoporous anodic aluminum oxide (AAO) templates have been used as shadow masks to fabricate regular nanodot arrays of a variety of materials, including Au, GaAs, InGaAs/GaAs, Ni, Si, and Er-doped Si,[21–24] since the size and separation of the pores can be easily controlled by varying the etching and oxidation conditions. Lee *et al.*[25] have recently developed a new process based on AAO to obtain gold nanotube membranes which were electrochemically produced by a one-step replication process of perfectly ordered nanoporous AAO templates.[26] In our previous work,[16] the gold nanotube membranes were used as shadow masks in order to deposit hexagonally ordered BLT nanostructure arrays.

In this paper we report on the detailed investigation of

[a]Electronic mail: sklee@mpi-halle.de

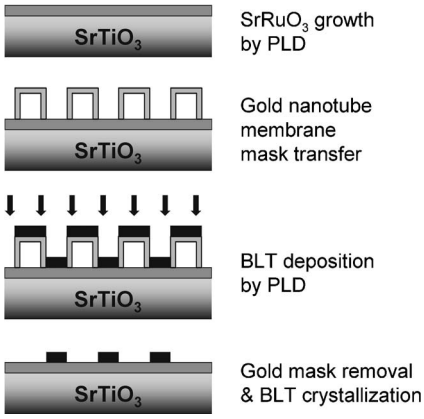

FIG. 1. Flow chart of the experimental procedure to fabricate periodic arrays of ferroelectric BLT nanostructures.

crystallography and anisotropic properties of ferroelectric BLT nanostructures of different crystallographic orientations grown on (001)-, (011)-, and (111)-oriented $SrTiO_3$ substrates covered with $SrRuO_3$ electrode layers by pulsed laser deposition (PLD).

II. EXPERIMENT

The whole fabrication process of periodic arrays of ferroelectric BLT nanostructures is schematically illustrated in Fig. 1. PLD was employed for the deposition of regular BLT nanostructure arrays on $SrRuO_3$-covered $SrTiO_3$ single crystal substrates, using gold nanotube membranes as shadow masks. This method has some advantages over other evaporation techniques, including the stoichiometric transfer of material from the target, in spite of the target involving complex stoichiometry, and the easy control of the deposition rate. In addition to the easy operation of the system and the wide range of possible materials to ablate, the widely variable pressure regime and the highly energetic impinging species are remarkable features that enable the formation of sharply bounded nanostructures on the substrate. The BLT nanostructures were deposited from a $Bi_{3.75}La_{0.75}Ti_3O_{12}$ pressed powder target, at room temperature of the substrate, and in an oxygen pressure of 1×10^{-4} mbar. PLD was performed employing a KrF excimer laser at a wavelength of 248 nm, a repetition rate of 5 Hz, and an energy density of 2.3 J/cm^2. After BLT deposition, the nanotube membranes were lifted off by a solvent-free mechanical process, and the BLT nanostructures were subsequently *ex situ* crystallized at 700 °C in a pure oxygen atmosphere. $SrRuO_3$ thin films, ~10 to 20 nm thick and grown by PLD, were used as bottom electrodes, also serving as epitaxial templates. The pseudocubic perovskite $SrRuO_3$ (a_c=0.3928 nm) proves to be a very good electrode material because it is well lattice matched with $SrTiO_3$ (a_c=0.3905 nm) and chemically compatible with the ferroelectric materials and the substrate.[27] More details concerning the $SrRuO_3$ deposition, the fabrication of BLT nanostructure arrays, and the preparation of gold nanotube membranes were described elsewhere.[16,25]

Crystallographic orientation and epitaxial relationships of the BLT nanostructure arrays were characterized by x-ray diffraction (XRD) pole figure analyses using a PANalytical X'Pert MRD four-circle diffractometer. Transmission electron microscopy (TEM) in cross section geometry using a Philips CM20T electron microscope was applied for microstructure characterization. The surface topography of the nanostructure arrays was investigated by atomic force microscopy (AFM) (Digital Instruments D5000) working in tapping mode using a standard silicon tip. Piezoelectric hysteresis loops as well as piezoresponse images in out-of-plane and in-plane modes were recorded by scanning force microscopy operating in piezoresponse mode (PFM) using a Thermomicroscope Autoprobe CP Research AFM.

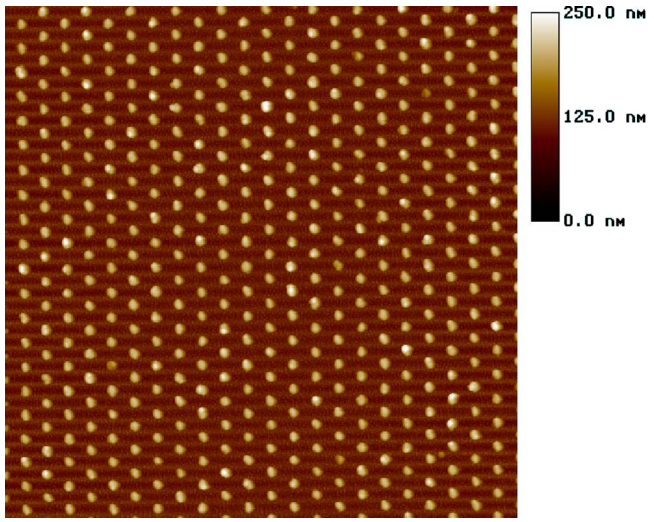

FIG. 2. (Color online) AFM topography image (image size: 10×10 μm^2) of a BLT nanostructure array as-deposited on a $SrRuO_3$-covered $SrTiO_3$ single crystal substrate using a gold nanotube membrane. Hexagonal arrangement of the BLT nanostructures with a center-to-center distance of 500 nm.

III. RESULTS AND DISCUSSION

The gold nanotube membranes[25] were used as shadow masks to generate the two dimensional arrays of ferroelectric nanostructures. Figure 2 shows an AFM image of a BLT nanostructure array as-deposited on a $SrTiO_3$ substrate covered with a $SrRuO_3$ electrode layer. A similar technique using closed-packed latex sphere monolayers as deposition masks to fabricate ferroelectric nanostructures was reported.[20] For that technique it is rather difficult to obtain large areas of well-ordered arrays. Due to the self-organization process many defects as stacking faults are present in the latex monolayer. However, using gold nanotube membranes we achieved a large area (typical area: $\sim10\times10$ mm^2) of perfectly well-ordered arrays of BLT nanostructures with hexagonal arrangement, as seen in Fig. 2. Individual BLT nanostructures were spatially apart by 500 nm. This distance is identical to the intertube distance of the gold nanotube membrane.[16]

AFM was employed to make a comparison between the sizes of the BLT nanostructures before and after annealing and to analyze the lateral and vertical dimensions. Figures 3(a) and 3(b) show AFM topography images of as-deposited and crystallized BLT nanostructures on $SrRuO_3$-covered $SrTiO_3$ substrates. Figures 3(c) and 3(d) represent corresponding section profiles. From these AFM investigations we

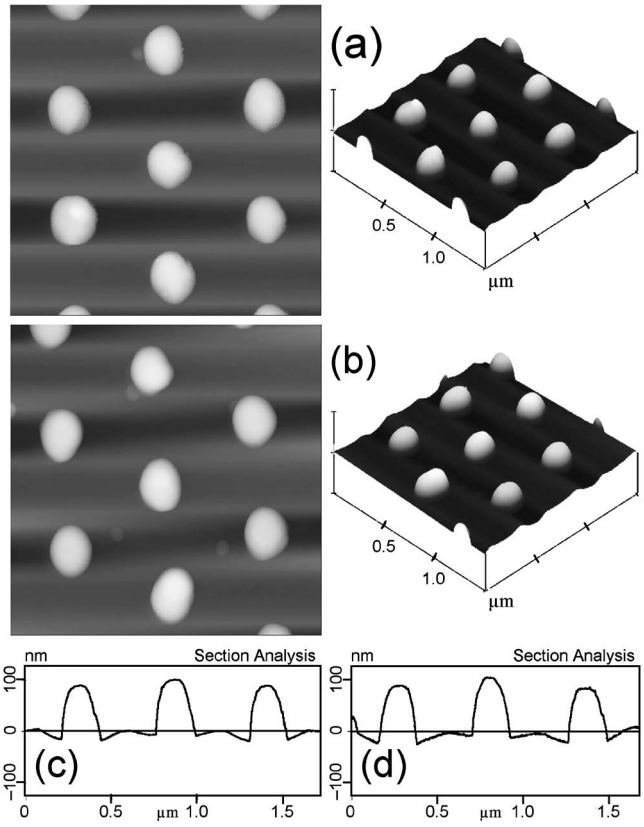

FIG. 3. Comparison of AFM topography images [(a) and (b)] (image size: $1.5\times1.5\ \mu m^2$) and corresponding section analysis profiles [(c) and (d)] between the as-deposited [(a) and (c)] and crystallized [(b) and (d)] BLT nanostructures. The height scale of the images range from 0 to 250 nm.

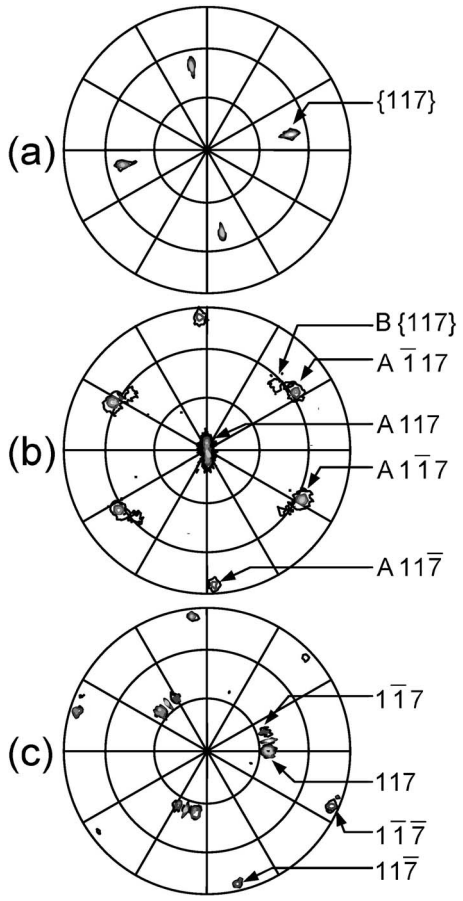

FIG. 4. X-ray diffraction pole figures of BLT nanostructures on (a) (001)-, (b) (011)-, and (c) (111)-oriented $SrTiO_3$ substrates covered with $SrRuO_3$ electrode layers. The fixed 2θ angle was 30.1° corresponding to the BLT 117 reflection. Peaks originating from (118)- and (100)-oriented parts of the BLT nanostructures are denoted "A" and "B," respectively in Fig. 4(b). The center and the rim of the pole figure correspond to ψ=0° and 90°, respectively.

observed that after annealing, the two dimensionally periodic arrays of the BLT nanostructures with hexagonal arrangement were retained, and no significant shrinkage or deformation was observed in the individual BLT nanostructures. Ferroelectric nanostructures fabricated by chemical solution deposition (CSD) generally show some deformation and shrinkage in their shape and size during the crystallization process.[17] Moreover, for $SrBi_2Ta_2O_9$ nanostructures on Nb-doped $SrTiO_3$(111) substrates produced by PLD, a shrinkage in vertical and lateral dimensions was reported because of a high crystallization temperature of 950 °C.[28] In most of the cases our BLT nanostructures have an oval shape, and their average height and lateral size are about 100 nm and about 150 nm, respectively. The oval shape might originate from either a somewhat elliptical shape of the gold nanotubes or from a small shadow effect that may occur during PLD deposition.

Although the BLT nanostructures were amorphous after lifting off the gold membrane, and then *ex situ* crystallized, we obtained epitaxial BLT nanostructures with definite orientation relations with respect to the underlying $SrTiO_3$ substrates. Due to the large area of the BLT nanostructure arrays, XRD measurements could be directly applied. Figure 4 shows XRD pole figures of BLT nanostructure arrays on (a) (001)-, (b) (011)-, and (c) (111)-oriented $SrTiO_3$ substrates covered with $SrRuO_3$ electrode layers of the same respective orientation. The fixed 2θ angle used to record the pole figures was 30.1° corresponding to the BLT 117 planes. As can be seen in Fig. 4(a), four reflection peaks with a fourfold symmetry are observed at $\psi\approx51°$ revealing a single-domain situation. From this pole figure, the BLT nanostructures on $SrTiO_3$(001) turn out to be (001)-oriented (*c*-axis-oriented) and have a good in-plane orientation. [Note that the BLT 117 planes have a tilt angle of 50.7° with respect to the BLT (001) plane, which is parallel to the substrate surface. ψ =90° corresponds to the substrate surface being parallel to the plane defined by the incident and reflected x-ray beam.]

The pole figure of the BLT nanostructures on the $SrRuO_3$(011)/$SrTiO_3$(011) substrate is more complicated, as can be seen in Fig. 4(b). First of all, it consists of a set of peaks (marked "A") that stem from a (118)-oriented part of the BLT nanostructures, and of another set (marked "B") which stems from a (100)-oriented part. Second, the peaks corresponding to the (118) orientation indicate the presence of two types of azimuthal domains. Peaks of set A are observed at $\psi\approx4°$, 65°, and 82° corresponding to 117, $\bar{1}17/1\bar{1}7$, and $11\bar{7}$ reflections from the (118)-oriented part of the BLT nanostructures [cf. the angles $\angle(118):(117)=3.8°$, $\angle(118):(\bar{1}17)=64.1°$, $\angle(118):(1\bar{1}7)=64.6°$, and $\angle(118):(11\bar{7})=82.4°$]. A detailed analysis reveals that the (118)-oriented BLT nanostructures occur with two azimuthal

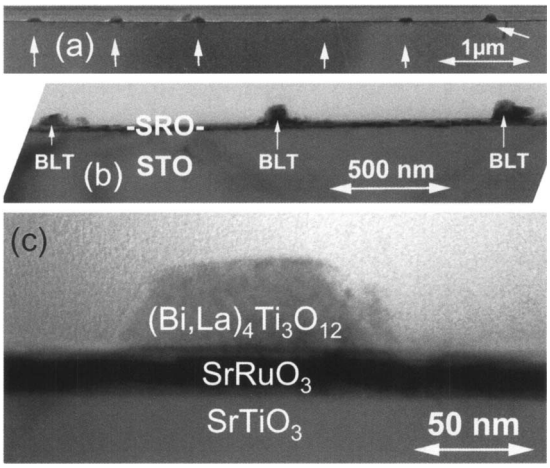

FIG. 5. Cross-sectional transmission electron micrographs of crystallized BLT nanostructure arrays of different orientations on $SrTiO_3$ substrates, taken with various magnifications.

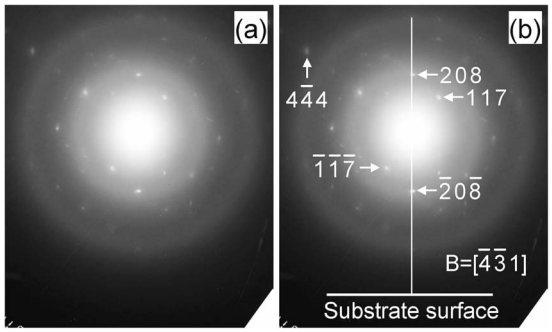

FIG. 6. (a) Cross-sectional SAED pattern taken from a (104)-oriented BLT nanostructure grown on a $SrRuO_3$-covered $SrTiO_3$(111) substrate. (b) Result of the quantitative evaluation of the diffraction pattern in terms of BLT spots. B is the direction of the electron beam.

domain variants, i.e., in exactly that double-twin situation which is well-known from (118)-oriented BLT thin films.[14] Set B appears at $\psi \approx 57°$ and consists of the 117, $1\bar{1}7$, $11\bar{7}$, and $1\bar{1}\bar{7}$ reflections from the (100)-oriented part of the nanostructure indicating that this part has a single-domain situation. We have also observed a mix of the (118) and (100) orientations in BLT thin films epitaxially grown on $SrTiO_3$(011) single crystal substrates covered with about 15 nm thick $SrRuO_3$ electrode layer.[29] Cross-sectional electron diffraction patterns (not shown) point to the additional presence of a minor (117) orientation of BLT as well.

Finally, in the case of BLT nanostructures on the $SrRuO_3(111)/SrTiO_3(111)$ substrate, a triple-twin situation was found as demonstrated by the pole figure shown in Fig. 4(c). The peaks at $\psi \approx 36°$ from the 117 and $1\bar{1}7$ reflections as well as at $\psi \approx 84°$ from the $11\bar{7}$ and $1\bar{1}\bar{7}$ reflections indicate the triple-twin situation, showing that the BLT (104) plane is parallel to the substrate plane, because the angle between the (104) and (117) planes of BLT is 36.4° [cf. the angles $\angle(104):(117)=36.4°$, $\angle(104):(1\bar{1}7)=36.4°$, $\angle(104):(11\bar{7})=84.1°$, and $\angle(104):(1\bar{1}\bar{7})=84.1°$].

Having a closer look at the three different pole figures, one can see shoulders of reflection peaks at $\psi \approx 45°$ [Fig. 4(a)], $\psi \approx 0°$ [Fig. 4(b)], and $\psi \approx 36°$ [Fig. 4(c)]. To demonstrate their origin, pole figures of only the corresponding $SrRuO_3$-covered $SrTiO_3$ substrates were recorded for the three different substrates (data not shown), at the same $2\theta = 30.1°$ corresponding to the BLT 117 planes as well. It turned out that the peaks with low reflection intensity in the pole figures of Fig. 4 most probably are $SrTiO_3$ 011 reflections because the used 2θ angle of the BLT 117 reflection is rather close to that of the $SrTiO_3$ 011 reflection. (The 2θ angle difference between BLT 117 and $SrTiO_3$ 011 planes is only about 2.3°.)

Figure 5 shows a series of cross-sectional TEM images of BLT nanostructures on different $SrRuO_3/SrTiO_3$ substrates at different magnifications. In evaluating these images, one has to keep in mind that during the sample preparation of cross-sectional specimens, some or all of the BLT nanostructures of a certain image may have not been cut along the middle of the nanostructures. In addition, the cut direction may not be exactly parallel to a line of the array, or may even cross different lines of the array. Occasional variations of the apparent spacing (pitch) between the nanostructures may have their origin in these effects. Figure 5(a) shows such a deviation from the otherwise regular spacing, in the middle of the image. Figure 5(b) shows some apparent, small variations of the shape of the nanostructures. Overall, Figs. 5(a) and 5(b) show, however, a rather uniform cell-to-cell shape and size. Figure 5(c) shows a BLT nanostructure with a height of about 40 nm and a width of about 120 nm, at somewhat higher magnification, revealing a trapezoidal shape projection. In addition, this TEM image shows a smooth $SrRuO_3$ bottom electrode layer with a thickness of about 20 nm.

Figure 6 shows a cross-sectional selected area electron diffraction (SAED) pattern taken from a single BLT island of a nanostructure array grown on a $SrTiO_3$(111) substrate. On the background of a diffuse ring pattern, which originates from the amorphous glue used to prepare the cross-sectional specimen, a rather regular spot pattern is visible. Because of the low volume of the island, the diffraction spots are weak. [For better visibility, the pattern is shown twice—once without indexing, Fig. 6(a), and once with, Fig. 6(b).] The orientation of the substrate surface is shown as a horizontal line in Fig. 6(b), whereas the vertical line marks the normal to the substrate. The 208, 000, and $\bar{2}0\bar{8}$ reflections are all on this vertical line, demonstrating the (104) orientation of the BLT nanostructure. Some of the other spots have also been indexed, which enabled the determination of the electron beam direction as BLT[$\bar{4}\bar{3}1$].

In order to investigate whether the crystallized BLT nanostructures show ferroelectric switching, piezoelectric hysteresis loops and piezoresponse images were recorded using PFM. Figure 7(a) shows a typical piezoelectric hysteresis loop recorded from a *c*-axis-oriented BLT nanostructure on a $SrRuO_3(001)/SrTiO(001)$ substrate. The measured value of the effective remanent piezoelectric coefficient ($2d_{zz}$) is 5.0 pm/V (positive $d_{zz}=-0.1$ pm/V and negative $d_{zz}=-5.1$ pm/V) for a maximum applied voltage of 5 V. A negative vertical shift of the piezoelectric hysteresis loop of ferroelectric nanostructures has been described before, and

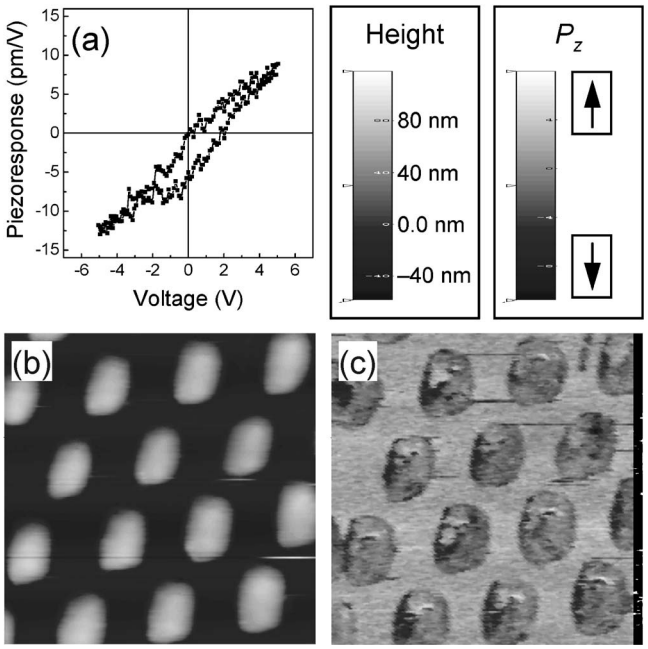

FIG. 7. (a) Piezoelectric hysteresis loop, (b) topography image, and (c) piezoresponse image (out-of-plane) of BLT nanostructures grown on a $SrRuO_3(001)$-covered $SrTiO_3(001)$ single crystal substrate. The image size of (b) and (c) is $1.5\times1.5\ \mu m^2$.

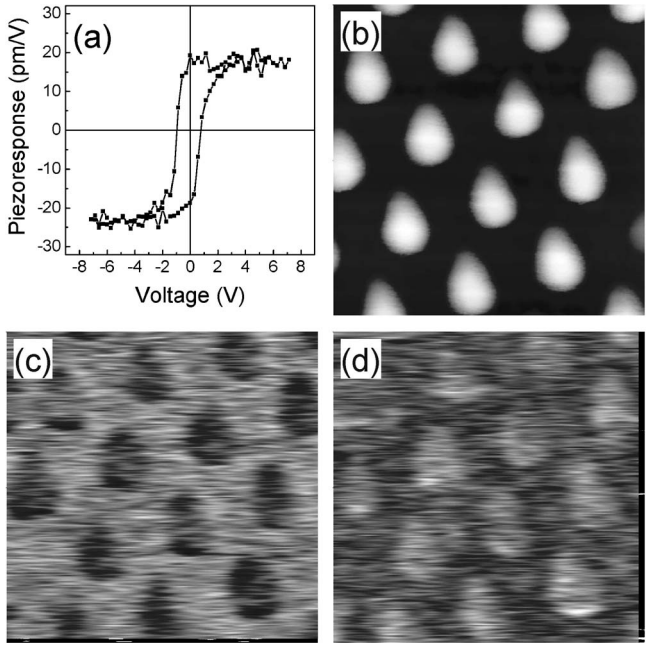

FIG. 8. (a) Piezoelectric hysteresis loop, (b) topography image, (c) out-of-plane piezoresponse image, and (d) in-plane piezoresponse image of BLT nanostructures grown on a $SrRuO_3(011)$-covered $SrTiO_3(011)$ single crystal substrate. The image size of (b) to (d) is $1.5\times1.5\ \mu m^2$.

has been discussed in terms of imprint due to interfacial effects.[6,30] As already well known, *c*-axis-oriented SBT films do not exhibit any ferroelectricity, but *c*-axis-oriented $Bi_4Ti_3O_{12}$ exhibits a distinct piezoelectric hysteresis loop with weak ferroelectricity.[31] Figures 7(b) and 7(c) show the typical surface morphology and the corresponding ferroelectric domain structure of BLT nanostructures, respectively. White and black contrast regions in the piezoresponse image generally correspond to positive (polarization upward) and negative (polarization downward) ferroelectric domains, respectively. The regions without a net black or white contrast correspond to areas of the sample that possess no piezoelectric behavior. The out-of-plane piezoresponse image in Fig. 7(c) reveals a weak contrast within each *c*-axis-oriented BLT nanostructure and almost no contrast in the $SrRuO_3$ electrode layer ("gray"). Due to the presence of the small component of the spontaneous polarization of BLT along the crystallographic *c* axis, the piezoelectric coefficient d_{zz} does not vanish. The weak contrast in *c*-axis-oriented BLT nanostructures indicates a small reversible switching of the polarization along their *c* axis.

Figures 8(a) and 8(b) show a well-defined piezoelectric hysteresis loop and AFM topography image recorded from a mixed (118)/(100)-oriented BLT nanostructure array. A considerably higher value of the effective piezoelectric coefficient ($2d_{zz}$) of 38 pm/V was obtained from the BLT nanostructures on the $SrRuO_3(011)/SrTiO_3(011)$ substrate than from those on $SrRuO_3(001)/SrTiO_3(001)$. In spite of the image noise, a uniformly strong contrast of the BLT nanostructures was observed in both out-of-plane [Fig. 8(c)] and in-plane [Fig. 8(d)] piezoresponse images due to the rather high piezoelectric coefficient. A similar effective piezoelectric coefficient (d_{zz}) of 19 pm/V has been reported in 1 μm thick polycrystalline $Bi_{3.25}La_{0.75}Ti_3O_{12}$ thin films made by CSD, determining the slope of field-induced strain loops.[32]

Figures 9(a) and 9(b) show a piezoelectric hysteresis loop and an AFM topography image recorded from (104)-oriented BLT nanostructures on a $SrRuO_3(111)$-covered $SrTiO_3(111)$ substrate, revealing a lower piezoelectric coefficient ($2d_{zz}=1.4$ pm/V) than for BLT nanostructures on $SrRuO_3(011)/SrTiO(011)$ and on $SrRuO_3(001)/SrTiO_3(001)$ substrates. This low piezoelectric coefficient is not consistent with the polarization value of bulk BLT because it has been already demonstrated that non-*c*-axis-oriented BLT films have a higher polarization component than *c*-axis-oriented ones. We suggest that the result might be explained by the investigation of the corresponding piezoresponse image. Compared with piezoresponse images of BLT nanostructures on $SrRuO_3(011)/SrTiO(011)$ substrates, an inhomogeneous contrast within individual BLT nanostructures is seen in both out-of-plane [Fig. 9(c)] and in-plane [Fig. 9(d)] piezoresponse images. This observation means that two different polarization states are present simultaneously and therefore a net polarization state is detected. For example, 90° *a-b* domains may be present. In addition, although the magnitude of the piezoresponse signal depends on the component of the spontaneous polarization normal to the substrate surface, the exact relationship $d_{zz}(\theta)$ (where θ is the angle between the measurement direction and the [001] crystallographic axis of the tested grain) is governed by the transformation rules of the whole piezoelectric tensor. The value of d_{zz} may be closely related to the component of the vector of polarization normal to the substrate surface, but is not directly proportional to it.[33] In addition, the effective piezoelectric coefficient d_{zz} depends not only on θ but also on the azimuthal angle ϕ (in-plane orientation).

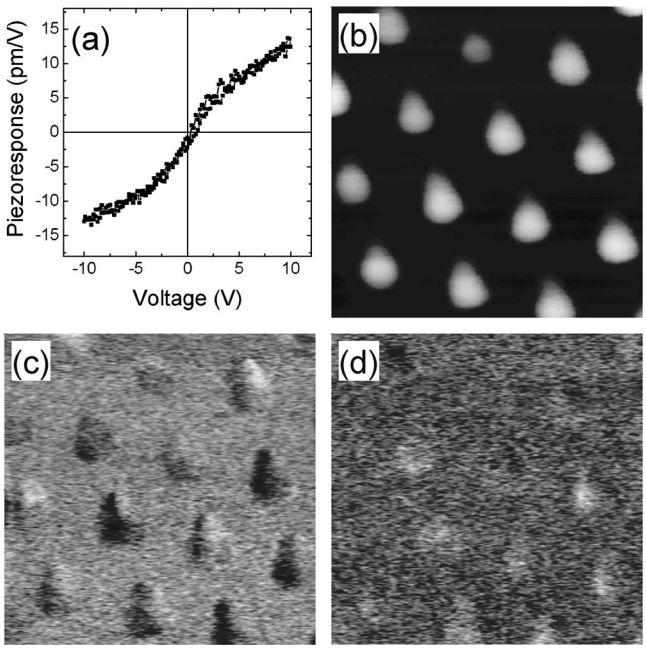

FIG. 9. (a) Piezoelectric hysteresis loop, (b) topography image, (c) out-of-plane piezoresponse image, and (d) in-plane piezoresponse image of (104)-oriented BLT nanostructures grown on a $SrRuO_3(111)/SrTiO_3(111)$ single crystal substrate. The image size of (b) to (d) is $1.5\times1.5\ \mu m^2$.

Harnagea *et al.* suggested the shape of the $d_{zz}(\theta,\phi)$ surface for $Bi_4Ti_3O_{12}$.[33] They calculated the $d_{zz}(\theta,\phi)$ surface as a function of the direction for monoclinic symmetry using piezoelectric coefficients obtained by Sa Neto and Cross.[34] According to their calculation, the piezoelectric surface showed that the maximum of the piezoelectric coefficient does not occur along the direction of the spontaneous polarization, but it has lobs protruding nearly along the *a* and *c* axes.

IV. CONCLUSIONS

In conclusion, well-ordered arrays of epitaxially twinned La-substituted $Bi_4Ti_3O_{12}$ nanostructures of (001), (118)/(100), and (104) orientations were achieved on $SrRuO_3$-covered $SrTiO_3$ substrates of (001), (011), and (111) orientations. Epitaxial BLT nanostructures with a height of about 100 nm and a lateral size of about 150 nm have been obtained. In spite of their small lateral size and thickness, the nanostructures of the arrays clearly revealed ferroelectric properties, the values of which depended on their crystallographic orientation. Among them, a maximum effective remanent piezoelectric coefficient ($2d_{zz}$) of about 38.0 pm/V was obtained in (118)/(100)-oriented BLT nanostructures on $SrRuO_3(011)$-covered $SrTiO_3(011)$ substrates. Although (104)-oriented BLT nanostructures showed a piezoresponse image contrast in both out-of-plane and in-plane images, revealing a switchable polarization, they exhibited a smaller piezoelectric coefficient ($2d_{zz}=1.4$ pm/V) than the others.

ACKNOWLEDGMENTS

M.A. gratefully acknowledges funding by the Volkswagoen Foundation through the "Nanosized ferroelectric hybrids" Project Nos. I/80897 and I/77738. W.L. and K.N. acknowledge support from BMBF (03N8701).

[1] C. A. P. de Araujo, J. D. Cuchiaro, L. D. McMillan, M. C. Scott, and J. F. Scott, Nature (London) **374**, 627 (1995).
[2] B. H. Park, B. S. Kang, S. D. Bu, T. W. Noh, J. Lee, and W. Jo, Nature (London) **401**, 682 (1999).
[3] H. N. Lee, D. Hesse, N. Zakharov, and U. Gösele, Science **296**, 2006 (2002).
[4] Y. S. Kim, D. H. Kim, J. D. Kim, Y. J. Chang, T. W. Noh, J. H. Kong, K. Char, Y. D. Park, S. D. Bu, J.-G. Yoon, and J.-S. Chung, Appl. Phys. Lett. **86**, 102907 (2005).
[5] M.-W. Chu, I. Szafraniak, R. Scholz, C. Harnagea, D. Hesse, M. Alexe, and U. Gösele, Nat. Mater. **3**, 87 (2004).
[6] M. Alexe, C. Harnagea, D. Hesse, and U. Gösele, Appl. Phys. Lett. **79**, 242 (2001).
[7] A. Gruverman, B. J. Rodriguez, A. I. Kingon, R. J. Nemanich, J. S. Cross, and M. Tsukada, Appl. Phys. Lett. **82**, 3071 (2003).
[8] J. Junquera and P. Ghosez, Nature (London) **422**, 506 (2003).
[9] A. D. Rae, J. G. Thompson, and R. L. Withers, Acta Crystallogr., Sect. B: Struct. Sci. **48**, 418 (1992).
[10] A. D. Rae, J. G. Thompson, R. L. Withers, and A. C. Willis, Acta Crystallogr., Sect. B: Struct. Sci. **46**, 474 (1990).
[11] J. Lettieri, M. A. Zurbuchen, Y. Jia, D. G. Schlom, S. K. Streiffer, and M. E. Hawley, Appl. Phys. Lett. **76**, 2937 (2000).
[12] J. Lettieri, M. A. Zurbuchen, Y. Jia, D. G. Schlom, S. K. Streiffer, and M. E. Hawley, Appl. Phys. Lett. **77**, 3090 (2000).
[13] T. Watanabe, H. Funakubo, and K. Saito, J. Mater. Res. **16**, 303 (2001).
[14] H. N. Lee and D. Hesse, Appl. Phys. Lett. **80**, 1040 (2002).
[15] A. Garg, Z. H. Barber, M. Dawber, J. F. Scott, A. Snedden, and P. Lightfoot, Appl. Phys. Lett. **83**, 2414 (2003).
[16] S. K. Lee, W. Lee, M. Alexe, K. Nielsch, D. Hesse, and U. Gösele, Appl. Phys. Lett. **86**, 152906 (2005).
[17] S. Okamura, K. Mori, T. Tsukamoto, and T. Shiosaki, Integr. Ferroelectr. **18**, 311 (1997).
[18] C. S. Ganpule, A. Stanishevsky, S. Aggarwal, J. Melngailis, E. Williams, R. Ramesh, V. Joshi, and C. P. de Araujo, Appl. Phys. Lett. **75**, 3874 (1999).
[19] I. Szafraniak, C. Harnagea, R. Scholz, S. Bhattacharyya, D. Hesse, and M. Alexe, Appl. Phys. Lett. **83**, 2211 (2003).
[20] W. Ma, C. Harnagea, D. Hesse, and U. Gösele, Appl. Phys. Lett. **83**, 3770 (2003).
[21] H. Masuda and M. Satoh, Jpn. J. Appl. Phys., Part 1 **35**, L126 (1996).
[22] X. Mei, D. Kim, H. E. Ruda, and Q. X. Guo, Appl. Phys. Lett. **81**, 361 (2002).
[23] J. Liang, H. Chik, A. Yin, and J. Xu, J. Appl. Phys. **91**, 2544 (2002).
[24] S. M. Park, C. H. Bae, W. Nam, S. C. Park, and J. S. Ha, Appl. Phys. Lett. **86**, 023104 (2005).
[25] W. Lee, M. Alexe, K. Nielsch, and U. Gösele, Chem. Mater. **17**, 3325 (2005).
[26] J. Choi, K. Nielsch, M. Reiche, R. B. Wehrspohn, and U. Gösele, J. Vac. Sci. Technol. B **21**, 763 (2003).
[27] C. B. Eom, R. J. Cava, R. M. Fleming, J. M. Phillips, R. B. van Dover, J. H. Marshall, J. W. P. Hsu, J. J. Krajewski, and W. F. Peck, Jr., Science **258**, 1766 (1992).
[28] W. Ma and D. Hesse, Appl. Phys. Lett. **85**, 3214 (2004).
[29] S. K. Lee, Ph.D. thesis, Martin Luther University Halle-Wittenberg, Halle, 2005.
[30] W. Ma and D. Hesse, Appl. Phys. Lett. **84**, 2871 (2004).
[31] C. Harnagea, A. Pignolet, M. Alexe, D. Hesse, and U. Gösele, Appl. Phys. A: Mater. Sci. Process. **70**, 261 (2000).
[32] H. Maiwa, N. Iizawa, D. Togawa, T. Hayashi, W. Sakamoto, M. Yamada, and S. Hirano, Appl. Phys. Lett. **82**, 1760 (2003).
[33] C. Harnagea, A. Pignolet, M. Alexe, and D. Hesse, Integr. Ferroelectr. **44**, 113 (2002).
[34] A. Sa Neto and L. E. Cross, J. Mater. Sci. **17**, 1409 (1982).